PAPER • **OPEN ACCESS**

Optimisation of deep drawn corners subject to hot stamping constraints using a novel deep-learningbased platform

To cite this article: H R Attar and N Li 2022 *IOP Conf. Ser.: Mater. Sci. Eng.* **1238** 012066

IOP Conf. Series: Materials Science and Engineering 1238 (2022) 012066 doi:10.1088/1757-899X/1238/1/012066

Optimisation of deep drawn corners subject to hot stamping constraints using a novel deep-learning-based platform

H R Attar*, N Li

Dyson School of Design Engineering, Imperial College London, London SW7 2DB, UK

*corresponding author E-mail: h.attar19@imperial.ac.uk

Abstract. State-of-the-art hot stamping processes offer improved material formability and therefore have potential to successfully form challenging components. The feasibility of components to be formed through these processes is dependent on their geometric design and its complex interactions with the hot stamping environment. In industrial practice, trial-anderror approaches are currently used to update non-feasible designs where simulation runs are needed each time a design change is made. These approaches make the design process resource intensive and require considerable numerical and process expertise. To demonstrate a superior approach, this study presents a novel application of a deep-learning-based optimisation platform which adopts a non-parametric geometric modelling strategy. Here, deep drawn corner geometries from different geometry subclasses were optimised to minimise wasted volume due to radii while avoiding excessive post-stamping thinning. A neural network was trained to generate families of deep drawn corner geometries where each geometry was conditioned on an input latent vector. Another neural network was trained to predict the thinning distributions obtained from forming these geometries through a hot stamping process. Guided by these distributions, the latent vector, and therefore geometry, was iteratively updated by a new gradient-based optimisation technique. Overall, it is demonstrated that the platform is capable of optimising geometries, irrespective of complexity, subject to imposed post-stamped thinning constraints.

1. Introduction

Lightweighting is one of the most effective strategies to reduce vehicle use-phase emissions [1] and therefore address the ever-growing concerns surrounding global environmental impact [2]. The latest hot stamping processes (e.g., the HFQ® process for high strength aluminium alloys [3]) are key enablers for realising vehicle lightweighting. However, there are several inherent manufacturing complexities associated with these processes. These include uneven cooling during stamping [4] and viscoplastic effects on the material flow stress at elevated temperatures [5]. These complexities create unfamiliarity among industrial designers and constrain the space of feasible component designs.

Published literature focuses on the development of advanced material models [5–8] that predict the material constitutive behaviour under hot stamping conditions. These models are then used to simulate hot stamping processes with high accuracy using Finite Element (FE) simulations [4]. However, these simulations usually take place late in design processes when the component geometry is near completion and require considerable numerical and process expertise.

Recently, researchers have started exploring time-efficient alternatives to FE simulations for component feasibility assessment. For simple approximations of complex geometries, Attar *et al*. [9] developed guidelines for quickly identifying if a designed geometry is likely to fall within a forming process's window of capability. For more complicated geometries with many geometric dimensions, non-parametric modelling representations offer a promising route. From the domain of machine learning,

researchers have explored using Convolutional Neural Networks (CNNs) as surrogate models of stamping processes. These models were able to rapidly predict post-stamping physical fields (e.g., thinning strain distribution) associated with a given die geometry as input [10–13]. Attar *et al*. [11] found that high accuracy in the predicted physical fields was achievable from CNNs when compared to FE simulations even for a complex hot stamping process.

However, these promising surrogate models are only capable of forward predictions without any backward feedback or guidance towards optimum designs. To address this drawback, Attar *et al*. [14] developed a novel deep-learning-based optimisation platform for optimising geometries subject to manufacturing constraints. The optimisation platform featured the interactions of two neural networks: 1) a geometry generator $f_{\theta 1}$ and 2) a manufacturing performance evaluator $g_{\theta 2}$. The geometry generator took advantage of recently developed implicit neural representations [15] but adapted for representing stamping geometries with high accuracy [14]. These representations made use of Signed Distance Fields (SDFs) which implicitly represent arbitrary geometries by their zero-level-sets and these geometries were extracted using Marching Cubes [16]. The manufacturing performance evaluator was a CNN-based surrogate model which used a 2D projection of the extracted geometries to predict their post-stamping physical fields. Manufacturing constraints were imposed based on these fields and were used to formulate objective functions to be minimised. The minimisation was performed by using the CNN-predicted manufacturability information to iteratively update the geometries until convergence.

The purpose of this paper is to present a novel engineering application of the aforementioned optimisation platform. This application offers practical guidance for researchers and industrial engineers who are planning to use the platform to develop geometries that are optimised for stamping applications.

2. Development of the geometry generator model

The procedures developed in [14] were employed here to establish a geometry generator model $f_{\theta 1}$. The definition of the geometries considered are first given followed by model details.

2.1. Geometry definition

The high level geometry class considered in this study was quarter deep drawn box corners. These corners are widely adopted on many rectangular or square shaped components, e.g., door inners in [17], but are challenging to successfully form [9]. Within this geometry class, three different geometry subclasses were defined and parameterised individually. These were named standard corners, chamfer corners and stepped sidewalls and can be seen in Figure 1. Different subclasses were used to showcase the non-parametric capability of the optimisation platform, as presented later in the paper.

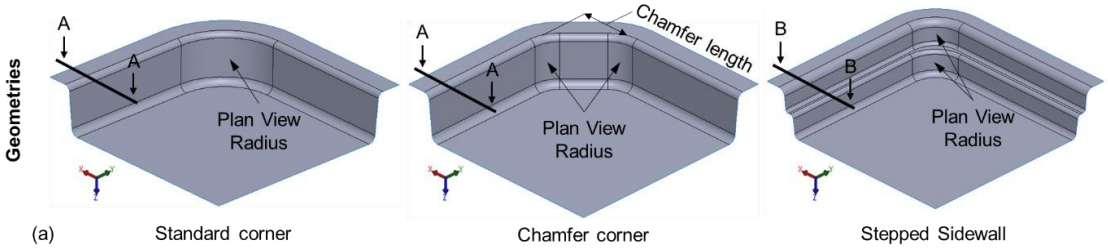

(a) Standard corner Chamfer corner Stepped Sidewall

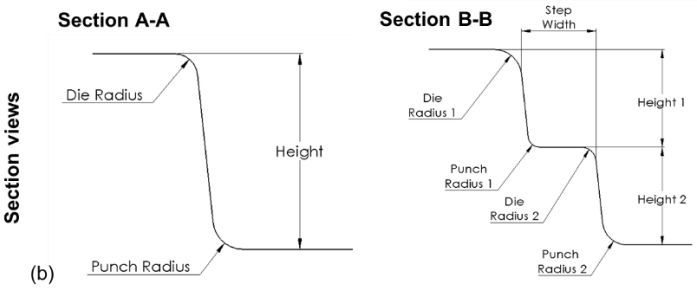

Figure 1. Definition of the three deep drawn box corner geometry subclasses considered in this study. Figure shows (a) 3D CAD views with corner parameters labelled and (b) section views with sidewall parameters labelled. Box half side length of 500 mm for all geometries.

2.2. Data preparation

The geometry generator model was trained to generate variants of die geometries from the geometry subclasses and this training process required example geometries. Using the CAD parameters shown in Figure 1, the Latin Hypercube design of experiments technique [18] and SolidWorks VBA was employed to generate these examples. For training data, a total of 1200 geometries were generated, 400 from each subclass. For test data, 300 geometries were generated, 100 from each subclass.

The generated geometries were then processed into a suitable form for neural network training. The top surface from each generated example die geometry was extracted in CAD software and exported as an STL surface mesh file, as shown in Figure 2(a). Each mesh was scaled such that the die edge was of unit length. The scaled meshes were then discretised into the point sets shown in Figure 2(b).

Figure 2. Data preparation for the geometry generator model. (a) Die geometries for training and test set exported from CAD software as STL surface meshes with zero thickness and unit edge length. (b) Surface meshes were discretised into two point sets: off surface and surface points. Surface points also had surface normal vectors. σ denotes the standard deviation of zero mean Gaussian noise.

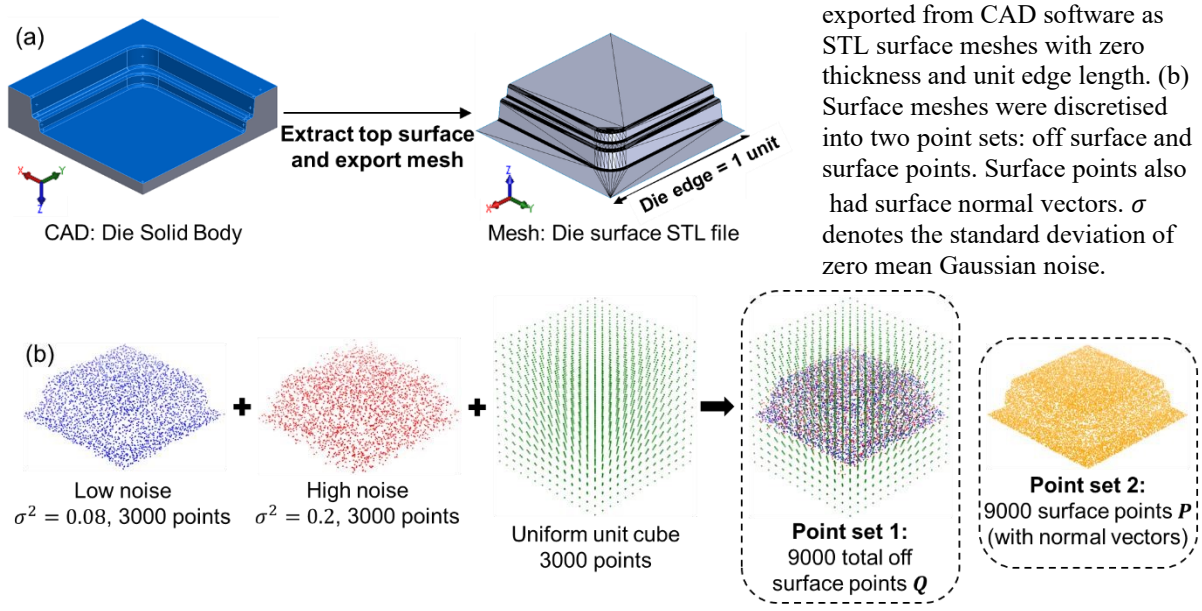

2.3. Model architecture

The architecture of the neural network model $f_{\theta 1}$ used as the geometry generator is shown in Figure 3. This model was based on an Auto-Decoder multilayer perceptron, recently introduced by Park *et al.* [15]. The model took as input a latent vector $\boldsymbol{z} \in \mathbb{R}^{128}$ which was concatenated with the coordinates of a 3D query point in ambient space $\boldsymbol{x} \in \mathbb{R}^3$. The output was a SDF value at the query point. Querying $f_{\theta 1}$ on a 3D grid of points enabled a volumetric SDF to be generated over that grid and this SDF was conditioned on the latent vector $\boldsymbol{z}$. Changing $\boldsymbol{z}$ during optimisation would change the generated SDF and therefore change the geometry implicitly represented by the zero-level-set of the SDF [15].

IOP Conf. Series: Materials Science and Engineering 1238 (2022) 012066 doi:10.1088/1757-899X/1238/1/012066

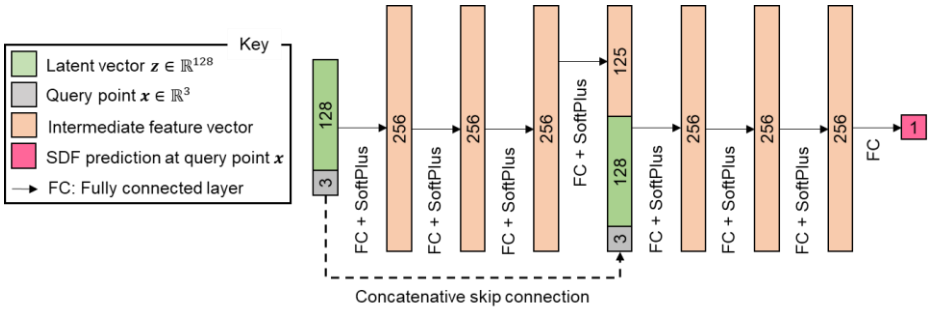

Figure 3. Architecture of the geometry generator neural network model $f_{\theta 1}$. Numbers denote vector length.

2.4. Training and inference

The training process of the model shown in Figure 3 followed the developments presented in [14]. The model was trained to generate an SDF given only the 3D coordinates of input points. Ground truth SDF values were not needed, and the model was instead trained to obey the geometric properties of SDFs. Attar *et al*. [14] found that this approach resulted in networks that were capable of high accuracy reconstructions of small geometric features on stamping geometries (e.g., tight radii).

To train the model in this way, a loss function to be minimised was formulated in terms of the network parameters θ_1 and the latent vectors for geometries in each training batch $\{\boldsymbol{z}_i\}^B_{i=1}$. This function is shown in Equation (1)

$$\arg\min_{\theta} \frac{1}{B}\sum_{i=1}^{B} \mathcal{L}_{\text{training}}(\theta_1, \boldsymbol{z}_i) = \arg\min_{\theta_1,\{\boldsymbol{z}_i\}_i^B} \frac{1}{B}\sum_{i=1}^{B} \left(\mathcal{L}_{\text{surface}}(\theta_1, \boldsymbol{z}_i) + \mathcal{L}_{\text{off surface}}(\theta_1, \boldsymbol{z}_i) + \mathcal{L}_{\text{reg}}(\boldsymbol{z}_i)\right) \quad (1)$$

where

$$\mathcal{L}_{\text{surface}}(\theta_1, \boldsymbol{z}_i) = \frac{1}{|\boldsymbol{P}|}\sum_{\boldsymbol{x}_j \in \boldsymbol{P}} \left(\lambda_1 \left|f_{\theta_1}(\boldsymbol{z}_i, \boldsymbol{x}_j)\right| + \lambda_2 \alpha_j \left\|\nabla_{\boldsymbol{x}_j} f_{\theta 1}(\boldsymbol{z}_i, \boldsymbol{x}_j) - \boldsymbol{n}_j\right\|_2\right) \quad (2)$$

$$\mathcal{L}_{\text{off surface}}(\theta_1, \boldsymbol{z}_i) = \frac{\lambda_3}{|\boldsymbol{Q}|}\sum_{\boldsymbol{x}_k \in \boldsymbol{Q}} \left(\left\|\nabla_{\boldsymbol{x}_k} f_{\theta 1}(\boldsymbol{z}_i, \boldsymbol{x}_k)\right\|_2 - 1\right)^2 \quad (3)$$

$$\mathcal{L}_{\text{reg}}(\boldsymbol{z}_i) = \lambda_4 \|\boldsymbol{z}_i\|_2 \quad (4)$$

A brief breakdown of Equation (1) is now given, and further details can be found in the original paper by Attar *et al*. [14]. The $\mathcal{L}_{\text{surface}}(\theta_1, \boldsymbol{z}_i)$ term was formulated on the surface point set $\boldsymbol{P}$ and contained two terms weighted by the scalars λ_1 and λ_2 as shown in Equation (2). Minimising the first term encouraged the generated SDF value at the geometry surface $f_{\theta 1}(\boldsymbol{z}_i, \boldsymbol{x}_j)$ to be zero, since SDFs should represent the surface geometry by their zero-level-sets [15]. Minimising the second term encouraged the spatial gradients of the generated SDF at the surface $\nabla_{\boldsymbol{x}_j} f_{\theta 1}(\boldsymbol{z}_i, \boldsymbol{x}_j)$ to be aligned with the surface unit normal vectors $\boldsymbol{n}_j$. This alignment of normals at the geometry surface is a geometric property of SDFs [14]. The α_j term gave a greater weighting to surface points belonging to tight geometry regions (e.g., tight radii) to encourage their accurate reconstruction.

The $\mathcal{L}_{\text{off surface}}(\theta_1, \boldsymbol{z}_i)$ term weighted by λ_3 was formulated on the off surface point set $\boldsymbol{Q}$. Minimising this term encouraged the spatial gradient of the generated off surface SDF $\nabla_{\boldsymbol{x}_k} f_{\theta 1}(\boldsymbol{z}_i, \boldsymbol{x}_k)$ to have unit magnitude, which is another property of SDFs [14]. Minimising the $\mathcal{L}_{\text{reg}}(\boldsymbol{z}_i)$ term weighted by λ_4

encouraged latent vector magnitudes that were concentred near the origin. This concentration enabled similar latent vectors for similar geometries and helped training convergence [15]. After training, high quality geometric reconstructions were enabled from $f_{\theta 1}$ on unseen test set geometries.

At inference time, the determined network parameters θ_1 were fixed and an optimum latent vector for an unseen geometry was inferred through an iterative optimisation procedure. This inference process involved minimising the expression shown in Equation (5) to obtain an optimal latent vector which best describes the unseen geometry.

$$\arg\min_{\boldsymbol{z}} \mathcal{L}_{\text{inference}}(\boldsymbol{z}) = \arg\min_{\boldsymbol{z}} \frac{1}{|\boldsymbol{P}|} \sum_{\boldsymbol{x}_j \in \boldsymbol{P}} \alpha_j \left\| \nabla_{\boldsymbol{x}_j} f_{\theta 1}(\boldsymbol{z}, \boldsymbol{x}_j) - \boldsymbol{n}_j \right\|_2 + \frac{\lambda_2}{|\boldsymbol{Q}|} \sum_{\boldsymbol{x}_k \in \boldsymbol{Q}} \left(\left\| \nabla_{\boldsymbol{x}_k} f_{\theta 1}(\boldsymbol{z}, \boldsymbol{x}_k) \right\|_2 - 1 \right) + \lambda_4 \|\boldsymbol{z}\|_2 \quad (5)$$

3. Development of the manufacturing performance evaluator model

An overview of the manufacturing performance evaluator model $g_{\theta 2}$ is presented and further details can be found by Attar *et al*. [11,12]. This model was a CNN based surrogate of the HFQ process [3] and was able to predict the post-stamped thinning distribution associated with an input die geometry.

3.1. HFQ stamping simulations

Simulations in PAM-STAMP were conducted to obtain target thinning distributions for the training and testing datasets of $g_{\theta 2}$. The CAD geometries described in Section 2.1. were converted into FE meshes for these simulations. The Python programming language was used to automate the loading of these meshes into PAM-STAMP and launch each simulation. The processing parameters were kept constant and set according to Attar *et al*. [14]. The temperature and strain rate dependent material model for AA6082 under HFQ conditions which was presented in [19] was used.

3.2. Model architecture and training

The Res-SE-U-Net architecture presented in Attar *et al*. [11,12] was used for $g_{\theta 2}$ and an overview of the manufacturability assessment using this model is presented in Figure 4. Specific details on the architecture of Res-SE-U-Nets can be found in the cited literature [11,12].

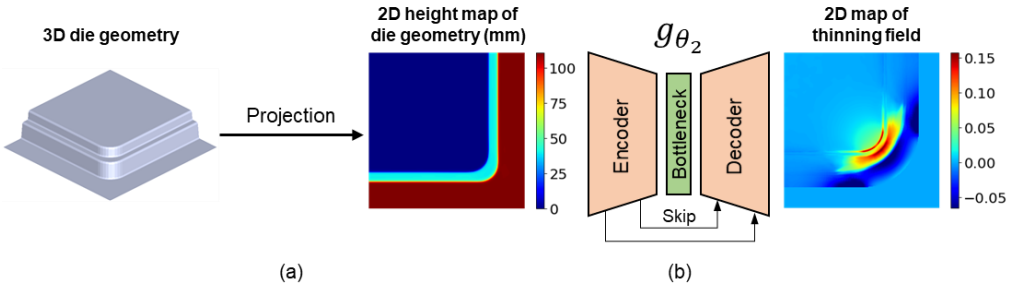

Figure 4. Overview of the manufacturing performance assessment approach. (a) 2D projection of 3D die geometry. (b) Thinning field prediction using CNN based surrogate model given the input height map.

The training data for $g_{\theta 2}$ consisted of input-target image examples like the one seen in Figure 4. For the input images, the 3D CAD geometries described in Section 2.1. were projected onto images to obtain 2D height maps. For the target images, the thinning distributions were first extracted from the HFQ stamping simulations and plotted onto the undeformed 2D blank nodes from the FE mesh. These 2D distributions were then linearly interpolated onto a uniform image grid.

$g_{\theta 2}$ was then trained in a supervised manner using the training data. Through an iterative optimisation process, the optimiser sought to find the combination of network parameters θ_2 such that the mean squared error (MSE) between target thinning distributions and network predictions was minimised. After training, high accuracy in thinning distribution predictions were seen from $g_{\theta 2}$ on unseen test set geometries.

4. Design optimisation

The optimisation platform was setup after $f_{\theta 1}$ and $g_{\theta 2}$ were established. An overview of the setup of the platform is presented in this section as well as details on two optimisation tasks.

4.1. Optimisation platform set up

Figure 5 shows the optimisation platform overview. The platform is based on the interaction of $f_{\theta 1}$ and $g_{\theta 2}$ and these networks are used to iteratively update the latent vector $\boldsymbol{z}$ to minimise $\mathcal{L}_{\text{task}}$.

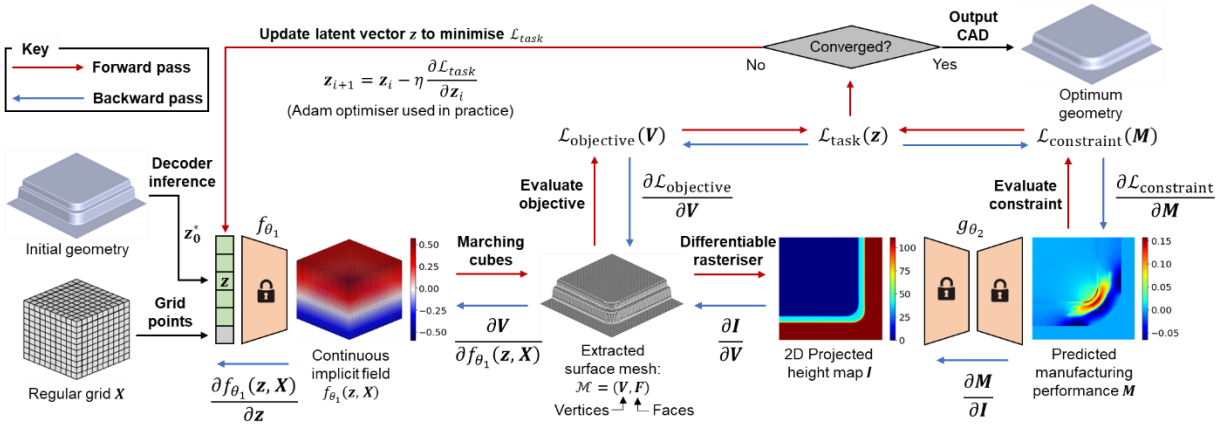

Figure 5. Optimisation platform overview. Padlocks on $f_{\theta 1}$ and $g_{\theta 2}$ denote fixed network parameters.

$\mathcal{L}_{\text{task}}$ was a function designed to be minimised and consisted of the summation of an objective function $\mathcal{L}_{\text{objective}}$ and a constraint function $\mathcal{L}_{\text{constraint}}$. These functions are task specific and were formulated based on the optimisation tasks considered in this study (see below). A forward pass through the platform occurred each optimisation iteration to compute $\mathcal{L}_{\text{task}}$ and update $\boldsymbol{z}$, as shown by the red arrows in Figure 5. $\boldsymbol{z}$ was iteratively updated by the Adam optimiser [20] by using a variation of the simplified gradient descent shown in Equation (6) where the subscript i denotes the ith optimisation iteration and η is a constant.

$$\boldsymbol{z}_{i+1} = \boldsymbol{z}_i - \eta \frac{\partial \mathcal{L}_{\text{task}}}{\partial \boldsymbol{z}_i} \tag{6}$$

A backward pass occurred each iteration to compute $\partial \mathcal{L}_{\text{task}}/\partial \boldsymbol{z}$ which was needed to perform the $\boldsymbol{z}$ updates as shown by the blue arrows in Figure 5. The chain rule was used to compute $\partial \mathcal{L}_{\text{task}}/\partial \boldsymbol{z}$ as shown in Equation (7). Details on the computation of these gradients are given by Attar *et al*. [14].

$$\frac{\partial \mathcal{L}_{task}}{\partial \boldsymbol{z}} = \left(\frac{\partial \mathcal{L}_{objective}}{\partial \boldsymbol{V}} + \frac{\partial \mathcal{L}_{constraint}}{\partial \boldsymbol{M}} \cdot \frac{\partial \boldsymbol{M}}{\partial \boldsymbol{I}} \cdot \frac{\partial \boldsymbol{I}}{\partial \boldsymbol{V}} \right) \cdot \frac{\partial \boldsymbol{V}}{\partial f_{\theta 1}(\boldsymbol{z}, \boldsymbol{X})} \cdot \frac{\partial f_{\theta 1}(\boldsymbol{z}, \boldsymbol{X})}{\partial \boldsymbol{z}} \tag{7}$$

4.2. Optimisation tasks

Two optimisation tasks were performed using the optimisation platform, one for a standard corner geometry and another for a stepped sidewall geometry. These tasks both involved optimising an initial geometry to minimise the wasted volume due to corner geometric features. Ideal geometries which have zero wasted volume would have infinitely sharp corners as shown in Figure 6. However, these geometries would impose large thinning defects and fractures during stamping [9]. To form these geometries successfully, their corner features must be carefully designed and optimised.

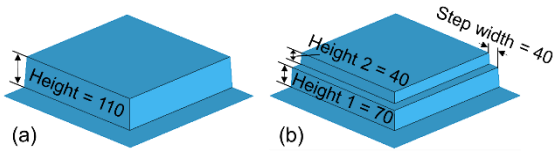

Figure 6. Ideal geometries for the optimisation tasks in this study. (a) Task 1 ideal geometry: Standard corner with no radii. (b) Task 2 ideal geometry: Stepped sidewall with no radii. Dimensions in mm.

The objective function $\mathcal{L}_{\text{objective}}$ and the constraint function $\mathcal{L}_{\text{constraint}}$ were first formulated for this optimisation problem. The formulation for $\mathcal{L}_{\text{objective}}$ is shown in Equation (8)

$$\mathcal{L}_{\text{objective}} = \lambda_1 \left(\sum_{\boldsymbol{x}_i \in \boldsymbol{P}_R} \min_{\boldsymbol{x}_j \in \boldsymbol{P}_I} \left\| \boldsymbol{x}_i - \boldsymbol{x}_j \right\|_2^2 + \sum_{\boldsymbol{x}_j \in \boldsymbol{P}_I} \min_{\boldsymbol{x}_i \in \boldsymbol{P}_R} \left\| \boldsymbol{x}_i - \boldsymbol{x}_j \right\|_2^2 \right) + \lambda_2 |H - H_{\text{ref}}| \tag{8}$$

where the bracketed term is the chamfer distance between point sets sampled from the ideal geometry $\boldsymbol{P}_I$ and the reconstructed geometry which is being optimised $\boldsymbol{P}_R$. These point sets are illustrated in Figure 7. A generous 30,000 points were sampled to approximate continuous surfaces. It is noteworthy that the generation of P_R occurred at each optimisation iteration and had to be done in a differentiable way to allow for $\partial \mathcal{L}_{objective} / \partial \boldsymbol{V}$ to be computed for Equation (7). In practice, the differentiable point sampler from the Pytorch3D framework was used for this purpose [21]. Weighting the chamfer distance by the scalar λ_1 formed the chamfer loss. Minimising the chamfer loss encouraged the geometry being optimised to be as close as possible to its idealised counterpart in Figure 6.

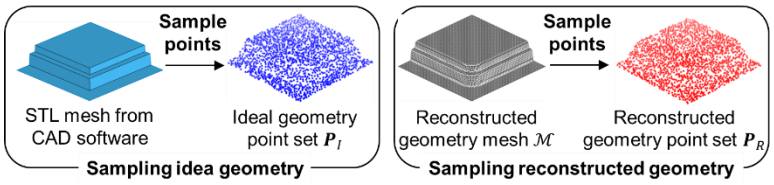

Figure 7. Illustration of point sets sampled from ideal geometry $\boldsymbol{P}_I$ and from the reconstructed geometry which is being optimised $\boldsymbol{P}_R$. These sets were used to compute the chamfer loss in Equation (8).

The second term in Equation (8) weighted by the scalar λ_2 was the height loss. Minimising this loss encouraged the height of the geometry being optimised H to be as close as possible to a desired reference height H_{ref}. Therefore, this loss ensured that where possible, optimisation of corner geometries were favoured over height. Here, $H_{\text{ref}} = 110$ mm as shown in Figure 6.

The formulation for $\mathcal{L}_{\text{constraint}}$ is shown in Equation (9)

$$\mathcal{L}_{\text{constraint}} = \lambda_3 \text{ReLU}(\max(\boldsymbol{M}(\boldsymbol{z})) - t_{\max}) \tag{9}$$

where λ_3 is a weighting scalar, $\boldsymbol{M}(\boldsymbol{z})$ is the generated post-stamping thinning field defined as

$$\boldsymbol{M}(\boldsymbol{z}) = g_{\theta 2}(\phi(f_{\theta 1}(\boldsymbol{z}, \boldsymbol{X}))) \tag{10}$$

where ϕ is the combined marching cubes [16] and differentiable rasteriser [21] steps in Figure 5. Here, ϕ can be thought of as a differentiable function that converts the volumetric SDF $f_{\theta 1}(\boldsymbol{z},\boldsymbol{X})$ into a 2D height map of the geometry encoded in $\boldsymbol{z}$. The non-differentiability of marching cubes [22] has recently

been addressed by Remelli *et al.* [23,24] and applied by Attar *et al.* [14]. The function ReLU $(x) := \max(0, x)$ was used in Equation (9) to make $\mathcal{L}_{\text{constraint}}$ inactive when the maximum thinning $\max(\boldsymbol{M}(\boldsymbol{z}))$ did not exceed a maximum allowable thinning constraint $t_{\max}$ and active otherwise.

4.2.1. Task 1 description and results. Task 1 was to optimise the initial chamfer corner geometry shown in Figure 8(b)(top). The objective of task 1 was to modify this geometry so that it is as close as possible to the ideal geometry shown in Figure 6(a) but subject to a 0.1 max thinning constraint. The results are shown in Figure 8.

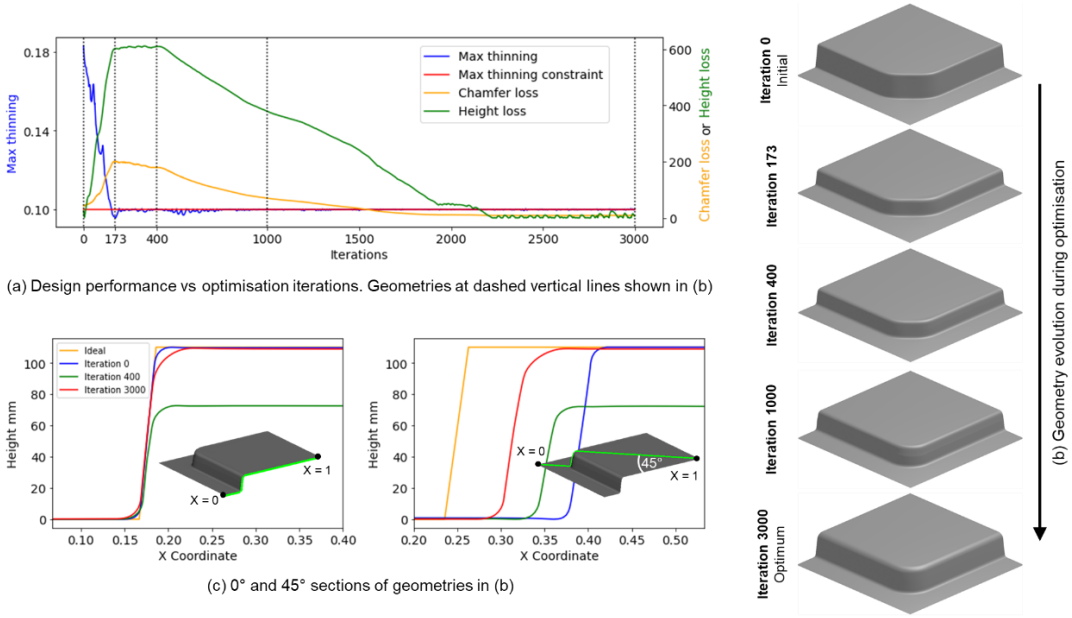

Figure 8. Optimisation task 1 results.

4.2.2. Task 2 description and results. Task 2 was to optimise the initial shallow standard corner geometry shown in Figure 9(b)(top). This shallow geometry could be, for example, one that might have been previously designed for a standard cold stamping process. Therefore, this task could be interpreted as optimising this geometry to take advantage of hot stamping capabilities that enable challenging features such as stepped sidewalls, tight radii and large draw depths [5,9]. The objective of task 2 was to modify this geometry so that it is as close as possible to the ideal geometry shown in Figure 6(b) but subject to a 0.2 max thinning constraint. The results are shown in Figure 9.

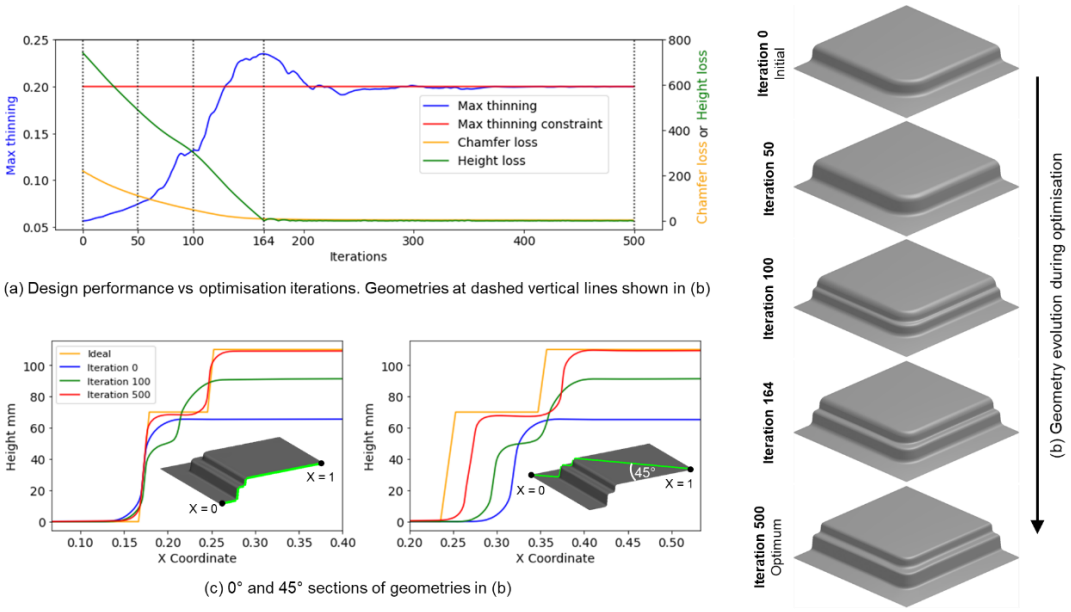

Figure 9. Optimisation task 2 results.

4.2.3. Discussion. The results for both tasks showed that expressive changes in geometries are possible. The optimisation history of task 1 is plotted on Figure 8(a). The maximum thinning was seen to decrease from 0.18 to 0.1 through the first 173 iterations and this decrease was mainly due to a reduction in geometry height as seen in Figure 8(b). At iteration 173, the constraint became inactive.

This formulation of Equation (9) prevented the constraint from becoming active again, as further explained by Attar *et al.* [14]. The remainder of the optimisation process was driven by minimising Equation (8). Any further geometric changes after iteration 173 occurred under constant maximum thinning at the constraint level. The final geometry at iteration 3000 was as close as possible to the ideal geometry in Figure 6(a) but with optimised corner features. The height loss in Equation (8) enabled the desired 110 mm height to be achieved but at the cost of larger radii.

An opposite scenario was seen for task 2. Figure 9(a) shows that the initial geometry had a maximum thinning of around 0.06 which was overly conservative since the allowable was set at 0.2. In this case, both the chamfer loss and the height loss proceeded to decrease with no manufacturing constraint since the constraint function in Equation (9) was inactive. Consequently, from iterations 0 to 164, height was increasing, the stepped feature was being introduced, and all radii were getting tighter. These changes resulted in increases in the maximum thinning which reached a maxima at iteration 164 but went back down to 0.2 shortly after. The final geometry at iteration 500 was as close as possible to the ideal geometry in Figure 6(b) but with optimised corner and stepped sidewall features.

The optimisation tasks were repeated with different constraint levels and the optimum geometries are shown in Figure 10. Noticeably tighter optimised corners can be seen when increasing maximum thinning constraint levels. At the strictest constraint level of 0.05, shallower geometries were obtained with larger radii and with no stepped feature for task 2. These results communicate understanding of feasible designs and design capabilities of a particular stamping process to industrial designers.

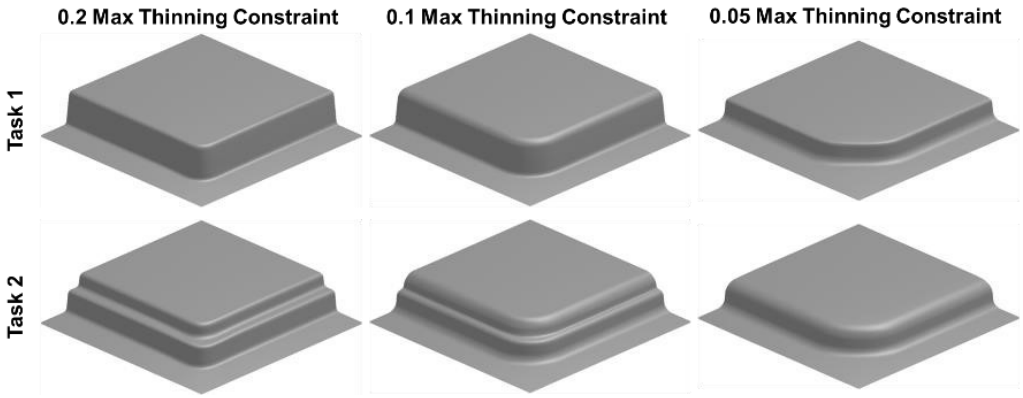

Figure 10. Optimum geometries from task 1 (top row) and task 2 (bottom row) for various maximum allowable thinning constraint values.

5. Conclusion

A novel application of a deep-learning-based platform for optimising sheet stamping geometries subject to manufacturing constraints was presented. Manufacturability-constrained optimisation of deep drawn corner geometries was performed to minimise wasted volume due to designed radii. Training details for two neural networks needed for the platform were given and these networks enabled non-parametric modelling and evaluation of sheet stamping geometries. The first network generated geometries and the second evaluated their manufacturing performance. New objective and constraint functions were formulated, and optimisation was performed by minimising these functions. It was demonstrated that expressive changes to geometries are possible using the optimisation platform. These changes were driven by achieving close to target designs while satisfying manufacturability and were irrespective of geometric complexity due to the deep-learning-based nonparametric approach. The presented application offers practical guidance for researchers and engineers who are planning to use the platform to develop optimum geometries for stamping processes. **Acknowledgments**

The authors thank Impression Technologies Ltd and the UK EPSRC for funding support.

References

[1] Raugei M, El O, Wang L, Lin J and Morrey D 2014 Life cycle assessment of the potential environmental benefits of a novel hot forming process in automotive manufacturing *J. Clean. Prod.* **83** 80–6

[2] UK gov 2020 *2018 UK Greenhouse Gas Emissions, Final figures*

[3] Lin J, Dean, Trevor A, Garrett, Richard P and Foster, Alistair D 2008 Process for forming aluminium alloy sheet component

[4] El Fakir O, Wang L, Balint D, Dear J P, Lin J and Dean T A 2014 Numerical study of the solution heat treatment, forming, and in-die quenching (HFQ) process on AA5754 *Int. J. Mach. Tools Manuf.* **87** 39–48

[5] Mohamed M S, Foster A D, Lin J, Balint D S and Dean T A 2012 Investigation of deformation and failure features in hot stamping of AA6082: Experimentation and modelling *Int. J. Mach. Tools Manuf.* **53** 27–38

[6] Shao Z, Li N, Lin J and Dean T 2017 Formability evaluation for sheet metals under hot stamping conditions by a novel biaxial testing system and a new materials model *Int. J. Mech. Sci.* **120** 149–58

[7] Lin J, Mohamed M, Balint D and Dean T A 2014 The development of continuum damage mechanicsbased theories for predicting forming limit diagrams for hot stamping applications *Int. J. Damage Mech.* **23** 684–701

[8] Wang A, Zheng Y, Liu J, El Fakir O, Masen M and Wang L 2016 Knowledge based cloud FE simulation a multi-objective FEA system for advanced FE simulation of hot stamping process *The 10th International Conference and Workshop on Numerical Simulation of 3D Sheet Metal Forming Processes*

[9] Attar H R, Li N and Foster A 2021 A new design guideline development strategy for aluminium alloy corners formed through cold and hot stamping processes *Mater. Des.* **207**

[10] Zimmerling C, Trippe D, Fengler B and Kärger L 2019 An approach for rapid prediction of textile draping results for variable composite component geometries using deep neural networks *AIP Conf. Proc.* **2113**

[11] Attar H R, Zhou H, Foster A and Li N 2021 Rapid feasibility assessment of components to be formed through hot stamping : A deep learning approach *J. Manuf. Process.* **68** 1650–71

[12] Attar H R, Zhou H and Li N 2021 Deformation and thinning field prediction for HFQ® formed panel components using convolutional neural networks *IOP Conf. Ser. Mater. Sci. Eng.* **1157** 012079

[13] Zhou H, Xu Q, Nie Z and Li N 2022 A Study on Using Image-Based Machine Learning Methods to Develop Surrogate Models of Stamp Forming Simulations *J. Manuf. Sci. Eng.* **144** 1–15

[14] Attar H R, Foster A and Li N 2022 Development of a deep learning platform for optimising sheet stamping geometries subject to manufacturing constraints *arXiv*

[15] Park J J, Florence P, Straub J, Newcombe R and Lovegrove S 2019 DeepSDF: Learning continuous signed distance functions for shape representation *arXiv*

[16] Lorensen W E and Cline H E 1987 Marching cubes: A high resolution 3D surface construction algorithm *Proc. 14th Annu. Conf. Comput. Graph. Interact. Tech. SIGGRAPH 1987* **21** 163–9

[17] Politis D J, Li N, Wang L, Lin J, Foster A D and Szegda D 2016 Prediction of Thinning Behavior for Complex-Shaped, Lightweight Alloy Panels Formed Through a Hot Stamping Process 395–401

[18] Bonte M H ., van den Boogaard A and Huétink J 2007 A Metamodel Based Optimisation Algorithm for Metal Forming Processes *Adv. Methods Mater. Form.*

[19] El Fakir O 2015 *Studies on the Solution Heat Treatment , Forming and in-Die Quenching Process in the Production of Lightweight Alloy Components* (Imperial College London)

[20] Kingma D P and Ba J L 2015 Adam: A method for stochastic optimization *3rd Int. Conf. Learn. Represent. ICLR 2015 - Conf. Track Proc.* 1–15

[21] Ravi N, Reizenstein J, Novotny D and Gordon T 2020 Accelerating 3D Deep Learning with PyTorch3D *arXiv*

[22] Liao Y, Donne S and Geiger A 2018 Deep Marching Cubes: Learning Explicit Surface Representations *Proc. IEEE Comput. Soc. Conf. Comput. Vis. Pattern Recognit.* 2916–25

[23] Remelli E, Lukoianov A, Richter S R, Guillard B, Bagautdinov T, Baque P and Fua P 2020 *MeshSDF: Differentiable Iso-Surface Extraction*

[24] Guillard B, Remelli E, Lukoianov A, Richter S, Bagautdinov T, Baque P and Fua P 2021 DeepMesh: Differentiable Iso-Surface Extraction *arXiv*